Understanding the spatial structure of RF-induced SOL modifications

2007 Plasma Phys. Control. Fusion 49 B35

(http://iopscience.iop.org/0741-3335/49/12B/S02)

Plasma Phys. Control. Fusion **49** (2007) B35–B45 doi:10.1088/0741-3335/49/12B/S02

Understanding the spatial structure of RF-induced SOL modifications

L Colas[1], A Ekedahl[1], M Goniche[1], J P Gunn[1], B Nold[1], Y Corre[1], V Bobkov[2], R Dux[2], F Braun[2], J-M Noterdaeme[2,6], M-L Mayoral[3], K Kirov[3], J Mailloux[3], S Heuraux[4], E Faudot[4], J Ongena[5], ASDEX Upgrade Team and JET-EFDA contributors[7]

[1] Association Euratom-CEA, CEA/DSM/DRFC, Centre de Cadarache, 13108 Saint-Paul lez Durance, France
[2] Max-Planck-Institut für Plasmaphysik, Boltzmannstrasse 2, D-85748 Garching, Germany
[3] Euratom–UKAEA Association, Culham Science Centre, Abingdon OX14 3DB, UK
[4] LPMIA, UMR 7040 CNRS, BP 239 F-54506 Vandoeuvre Cedex, France
[5] ERM-KMS, Association EURATOM-Belgian State, Brussels
[6] EESA Department, Gent University, B-9000 Gent, Belgium

Received 6 July 2007
Published 14 November 2007
Online at stacks.iop.org/PPCF/49/B35

Abstract
This paper summarizes recent experimental characterization of radio frequency (RF)-induced scrape-off layer (SOL) modifications in ASDEX-Upgrade (AUG), JET and Tore Supra (TS). Geometrical aspects are emphasized: complex SOL patterns are observed by several indicators visualized in one or two dimensions transverse to the magnetic field lines. Results are ascribed to inhomogeneous RF-induced SOL biasing around powered ion cyclotron range of frequencies antennas and associated $\boldsymbol{E} \times \boldsymbol{B}_0$ density convection (D'Ippolito *et al* 1993 *Phys. Fluids* B **5** 3603). Within a simple RF sheath model (Perkins 1989 *Nucl. Fusion* **29** 583), the shape of convective cells on TS can be interpreted in terms of RF-sheath generation by parallel RF currents. Some lessons are drawn for future machines.

(Some figures in this article are in colour only in the electronic version)

1. Introduction

Since the first use of ion cyclotron range of frequencies (ICRF) heating systems in magnetic fusion devices, the non-linear physics of ICRF waves in the plasma edge has attracted considerable attention. Early experiments were reviewed in [25, 26]. With the prospect of ITER, the topic has recently gained renewed interest. ICRF was applied in all-metal machines

[7] See appendix of Watkins M L *et al* 2006 *Proc. 21st Int. Conf. on Fusion Energy 2006 (Chengdu, 2006)* (Vienna: IAEA).

(on AUG [3, 12], Alcator C-mod [35, 36]), where RF-enhanced sputtering might contaminate the core plasma with high-Z impurities. Besides, a spurious phenomenon can be tolerable over transient times because of its modest amplitude, but can become harmful over long RF pulses (on LHD [31] or Tore Supra (TS) [7]) due to spatial localization or long-time accumulation. Finally ICRF was combined with other subsystems, such as lower hybrid current drive ((LHCD) on TS [14], JET [13, 21] and Alcator C-mod [34]). The operational density range at the LH launcher mouth is bounded by a trade-off between reasonable wave coupling and tolerable heat fluxes onto the launcher. ICRF-induced scrape-off layer (SOL) density modifications therefore impact on LH operation.

This paper summarizes recent measurements of RF-induced SOL modifications on AUG, JET and TS, with emphasis on their spatial structure. Spatial localization of the ICRF antenna-plasma interaction has been noticed frequently, e.g. in [3, 26, 32, 35]. Visualizing the RF-induced complex SOL patterns, in relation to the topology of RF currents over antenna components facing the plasma (or 'front face'), now becomes important. Firstly, recovering the measured SOL patterns imposes a severe constraint on interpretative physics models, which have so far been scarcely benchmarked in realistic geometry. Secondly, an accurate LH launcher positioning in the highly inhomogeneous ICRF antenna environment is essential for high power combined scenarios [14, 21]. Finally, geometry provides hints for front face design improvement [6], judicious port allocation [14] and clarifies which plasma facing components should be protected in future machines (e.g. [7, 31, 35]).

The paper first presents indirect indications of ICRF-induced inhomogeneous SOL changes: localized sputtering yield enhancement, asymmetric LH launcher behavior. Then SOL parameters are mapped in two dimensions (2D) transverse to magnetic field lines, first using the LH grill properties and then more directly with a reciprocating probe combined with a scan of the edge safety factor $q(a)$. The final section synthesizes the experimental results, proposes elements of interpretation and draws lessons for future machines.

2. Localized RF-induced sputtering yield enhancement

The fast magnetosonic wave used for ICRF heating is launched into the plasma from phased arrays of poloidal radiating straps. The TS antenna (shown in the inset of figure 6) and the AUG antenna include two straps, whilst the existing JET antennas have four. In the experiments described in this paper, antisymmetric strap phasing [0,π] was used, in a D(H) minority heating scenario, unless otherwise stated. On the TS and AUG antennas, as well as on the new JET-EP and the ITER antennas, the straps are housed in individual boxes, partially closed on the plasma side by a tilted Faraday screen meant to reduce the parallel RF electric field $E_{\|\mathrm{RF}}$. Antennas are protected from plasma influx by side limiters. All these front face components carry RF currents and contribute *a priori* to the antenna–plasma interaction.

Since 2006, 85% of the plasma facing components in AUG have been tungsten coated, including ICRF antenna poloidal limiters. Dedicated spectroscopic observations monitor tungsten erosion on several poloidal lines of sight, aiming either at an antenna limiter or a magnetically connected guard limiter [12]. In ICRF-heated discharges, the antenna limiter systematically exhibits both higher tungsten fluxes and higher effective sputtering yields Y^{eff} than with neutral beams [3, 12]. Figure 1 shows that the Y^{eff} increase is well correlated with the ratio of ICRH power over hydrogen recycling flux density. Y^{eff} is an indicator of primary ion energy, whose increase was estimated between 1 and 100 eV. Sputtering is enhanced with [0, $\pi/2$] strap phasing, especially on high triangularity plasmas [3]. Comparison of poloidal lines of sight suggests higher Y^{eff} towards the top of the antenna than near the equatorial plane. The ratio Y^{eff}(antenna)/Y^{eff}(guard) was used to quantify the degree of localization of

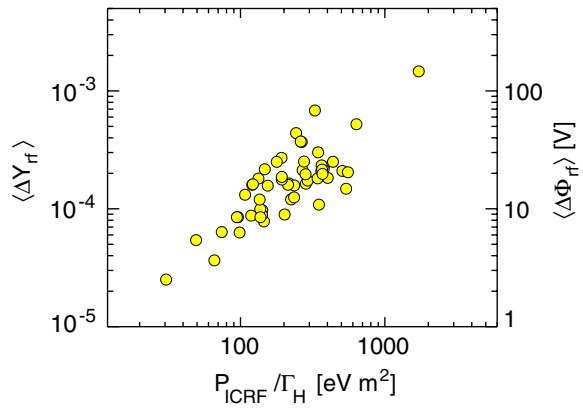

Figure 1. Scaling of the sputtering yield increase on the antenna side limiter of AUG ICRF antenna with the ratio of ICRH power over the hydrogen recycling flux density $P_{\mathrm{ICRH}}/\Gamma_{\mathrm{H}}$. Estimate of associated sheath potential enhancement. From [12].

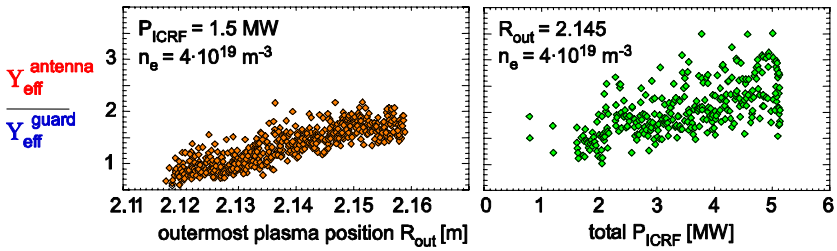

Figure 2. Degree of localization of RF-induced W sputtering on AUG. (*a*) Dependence on outermost plasma position; (*b*) dependence on RF power. Adapted from [4].

RF-induced interaction with the plasma [4]. Figure 2 shows higher localization with higher ICRF power and smaller antenna–plasma distance. At the same time the absolute tungsten influx and Y^{eff} were higher. To reduce the sputtering yield, a low plasma temperature at the limiters was found preferable and was obtained at high density.

On Alcator C-mod, enhanced molybdenum erosion was observed mainly at the end of open field lines passing in front of ICRF antennas, rather than on flux tubes intersecting the antenna limiters [35, 36]. Iron and copper radiation was monitored during ICRF on TS [23]. The level of intrinsic impurities was seen to increase practically linearly with the total injected power. Over a scan of H minority concentration a local minimum was found in metallic impurity brightness. Enhanced sheath potentials were suspected, rather than fast ions accelerated by ICRF waves and escaping from the plasma core, due to low sputtering yields at energies of several 100 keV. Although the source of metallic impurities could not be located spatially with precision, the Faraday screens or the main vacuum chamber are likely candidates.

3. Asymmetric LH launcher behavior during ICRH

LH waves are launched into the plasma by phased waveguide arrays. The inset of figure 4 shows the TS grill and figure 5 the JET launcher. LH wave coupling is characterized by a power reflection coefficient C_{ref} that is sensitive to the local density in front of the waveguides. Wave coupling therefore sets a lower limit to the operational density range at the LH launcher

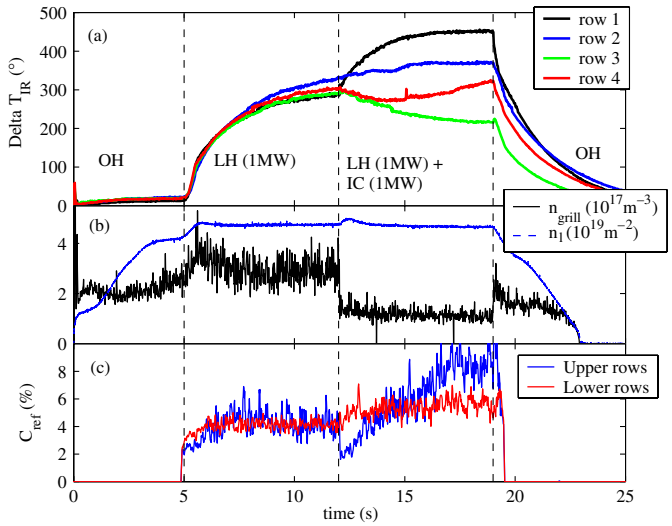

Figure 3. LH grill behavior during combined LHCD + ICRF pulse on TS. (*a*) Surface temperature elevation on left side limiter, in front of each waveguide row (Row numbering: see figure 4); (*b*) local density n_{grill} measured by dome Langmuir probe (connected to row 3) and line-integrated core density n_l; (*c*) power reflection coefficient averaged over upper and lower LH modules.

mouth. An upper bound is imposed by heat fluxes. Electron acceleration in the LH parallel near the field produces localized heat loads at both extremities of open field lines passing in front of each waveguide row [17, 30]. For a given LH launcher geometry and fixed parallel refractive index, the parallel heat flux $Q_{\parallel}$ increases with the local density and with the LH near field magnitude [16, 17]. This field magnitude is determined by the launched power and by C_{ref} (i.e. density again). The surface temperature elevation ΔT_{IR} on the actively cooled side limiters of the TS grill is monitored by infrared cameras [19] and serves as a sensor in a real-time safety system [24] to prevent over-heating in high power discharges [14]. In thermal steady-state, ΔT_{IR} is proportional to $Q_{\parallel}$.

Figure 3 shows the typical time history of the TS LH launcher properties over a combined ICRH+LHCD pulse. In this discharge, the line-averaged core density was feedback-controlled on interferometer measurements. Except for a small overshoot at the beginning of the ICRF pulse, it remained constant, insensitive to local SOL density modifications. In the ohmic phase, the left side limiter of the LH grill remained cool. At $t = 5$ s the grill was powered alone. Hot spots appeared in front of the waveguide rows on the left side limiter. All four zones reached similar steady-state temperatures in typically 7 s. LH coupling was also poloidally homogeneous over the launcher front face. When ICRH was added at $t = 12$ s, from an antenna next to the LH launcher, both LH coupling and heat loads were modified. Furthermore ΔT_{IR} evolution became poloidally asymmetric: some waveguide rows heated up and others cooled down. The LH coupling showed different evolutions on the top and bottom parts of the launcher. The local density n_{grill} in the LH launcher vicinity was measured by a fixed dome Langmuir probe located in the equatorial plane on the grill and connected magnetically to waveguide row #3 (see inset of figure 4). When ICRH was applied, n_{grill} dropped in less than 15 ms on the Langmuir probe. Such a fast timescale is smaller than the core particle confinement time and is only compatible with edge transport.

The TS LH launcher is mobile radially. In order to re-optimize C_{ref} and ΔT_{IR} on combined ICRH + LHCD scenarios, the radial gap from the LH grill to the separatrix was scanned over

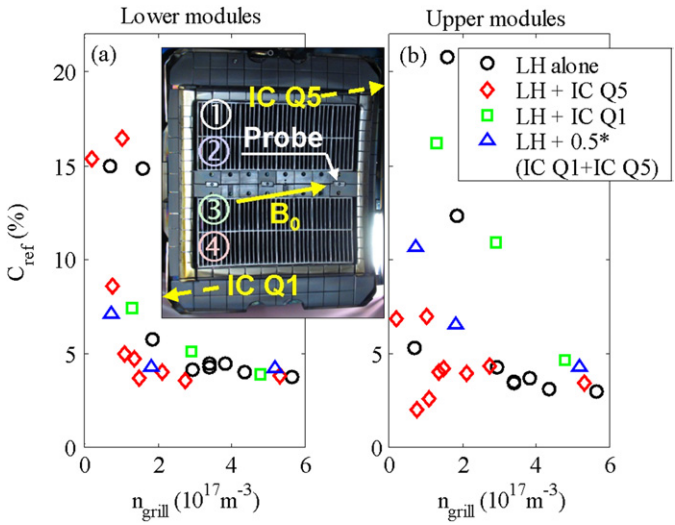

Figure 4. LH power reflection coefficient C_{ref} versus local density n_{grill} measured by dome Langmuir probe on the equatorial plane of LH grill on TS. Measurements obtained over a radial scan of LH grill by 12 mm, for different combinations of neighboring ICRF antennas Q1 and Q5. (*a*) average over lower LH modules; (*b*) average over upper modules. Inset: photograph of LH grill, with location of Langmuir probe and neighboring ICRF antennas, sketch of magnetic field line pitch and waveguide row numbering for figure 3.

12 mm from shot to shot. No other object was moved. Plasma discharges were similar to figure 3. Figure 4 summarizes LH coupling properties over the scan and for several combinations of two ICRF antennas surrounding the LH launcher. Total ICRF power of 1 MW was applied, with different power splittings. C_{ref} is plotted versus the local density n_{grill} measured by the fixed Langmuir probe. Figure 4(*a*) shows that, on lower LH modules, all measurements lie on a characteristic curve. C_{ref} is low at high density and progressively increases as n_{grill} drops below the cut-off density for the slow wave (1.7×10^{17} m^{-3} at 3.7 GHz). Interaction with ICRH displaces C_{ref} values towards the low density part of the characteristic curve. The magnitude of local density reduction depends on the antenna combination and on the grill radial position. A third ICRF antenna is installed on TS. It is not connected magnetically to the grill and never influences C_{ref}. All these observations point again to a localized RF-induced SOL modification rather than a global effect. This tendency, first evidenced on JET and TS [13] is also observed on Alcator C-mod [34]. While C_{ref} on lower modules always remains correlated with n_{grill} when ICRH is applied, a larger scatter appears on upper modules on figure 4(*b*), either towards better or worse LH coupling. It is speculated that n_{grill} is no longer representative of the local density in the upper part of the grill that is not connected to the Langmuir probe. In particular the upper modules could sometimes experience a local density *increase* during ICRH instead of the local *depletion* measured by the probe.

LH wave coupling asymmetry is even more striking on the JET LH grill, whose six rows of waveguides offer more spatial resolution than on TS. LH coupling is modified by the two ICRF antennas magnetically connected to the grill and not by two similar antennas located further away toroidally [21]. One antenna is usually not connected to the upper part of the LH grill. Therefore it does not affect the coupling of the upper rows whilst C_{ref} on the bottom three rows are larger at higher power on that antenna. Degradation of the coupling is generally observed when the other connected antenna is turned on. C_{ref} always increases with the

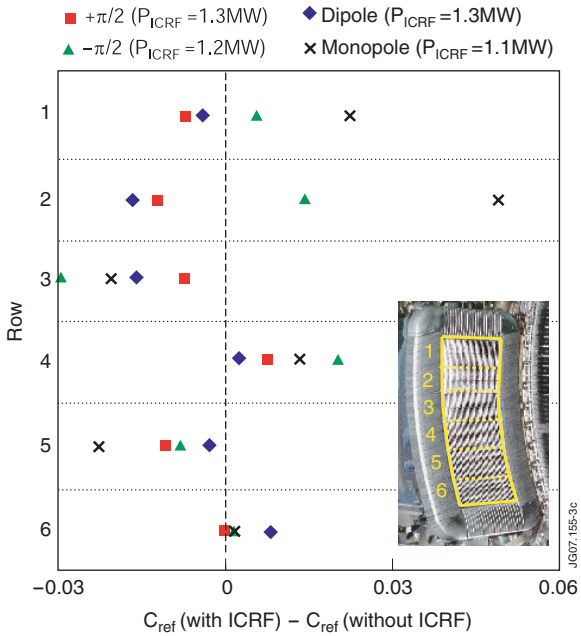

Figure 5. Variation of reflection coefficient during ICRF, averaged over each row of the JET grill, in combined pulses with connected ICRF antennas A and B and for four strap phasings. Plasma parameters were as follows: magnetic field 2.6 T; plasma current 1.5 MA; L-mode; LH launcher position 2.5 cm behind limiters; 7×10^{21} e^-/s D_2 puffed from near gas pipe. Inset: photograph of JET LH launcher with row numbering from top to bottom.

distance between the launcher and the limiter. However, opposite variations of C_{ref} may occur on different waveguide rows when ICRF is applied, including local coupling improvement. Poloidal as well as toroidal asymmetries were found, partly due to a mismatch of the plasma poloidal shape with the grill curvature. The LH coupling clearly depends on RF antenna phasing. Figure 5 shows that C_{ref} increases when antenna B is powered in $-\pi/2$ or monopole phasing, as compared with dipole and $+\pi/2$. Strong differences in C_{ref} behavior suggest that the local electron density modifications are not poloidally symmetric. Gas puffing from a nearby gas injection module was shown to improve LH coupling in combined pulses: it compensates density depletion by local ionization. This technique is now routinely used in experiments that require power from LHCD and connected ICRF antennas [13, 21].

4. 2D SOL mapping using LH launcher properties

The above experiments showed that optimization of the LH grill operation might be complicated during ICRF by large density gradients and poloidal asymmetry. It is therefore crucial to visualize the density patterns around ICRF antennas in 2D transverse to magnetic field lines, using C_{ref} and ΔT_{IR} as indicators.

The dataset of figure 4 was mapped in 2D in figure 6 as a function of the connection point of field lines emerging from the LH modules in a reference poloidal plane containing the septum of the powered ICRF antenna. Connection points are labelled by their altitude Z and their radial distance δr to ICRF antenna limiters (see inset). Radial resolution was obtained by displacing the grill radially, while vertical resolution was provided by the two series of

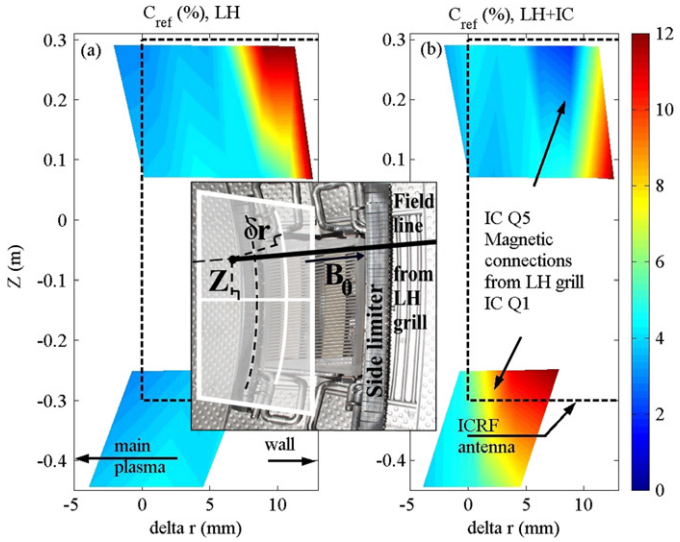

Figure 6. 2D map of LH power reflection coefficient on TS grill, for the set of RF pulses in figure 4. (*a*) with LH grill powered alone (1 MW); (*b*) LH (1 MW) combined with 1 MW ICRH from connected antenna (either Q1 left or Q5 right to LH grill). The same color scale is used in both panels. The vertical dashed line represents the leading edge of the ICRF side limiter and the horizontal dashed lines represent the vertical extent of the ICRF antenna box. Inset: photograph of TS ICRF antenna and sketch of the 2D coordinate system used for mapping in the reference plane.

LH modules connected to two ICRF antennas. Due to their pitch angle at $q(a) = 5.2$, field lines from the LH grill explore the upper part of the ICRF antenna located to the right of the LH launcher and the lower part of the antenna on its left (see figure 4). These two regions are featured by two coloured areas on figure 6. When the LH grill is radially 1 cm behind the antennas, LH coupling is initially difficult but improves during ICRF on waveguides connected to the upper part of the active antenna. On these waveguides, C_{ref} first increases and then drops as the grill is retracted away from the plasma. This suggests a local density minimum over the radial scan during ICRF. On lower waveguide rows, C_{ref} grows monotonically with increasing distance to the plasma and correlatively n_{grill} on the Langmuir probe decreases monotonically.

Similarly the steady-state temperature elevation ΔT_{IR} on the LH launcher side limiter was mapped in 2D. Figure 7(*a*), obtained with LH grill powered alone, shows moderate ΔT_{IR} with limited radial and poloidal variations. In figure 7(*b*), depending on magnetic connections to the powered antenna, both the temperature increase and decrease can be measured over the same combined RF pulse, resulting in large poloidal and radial gradients (up to 500 °C cm^{-1}). Strangely, when waveguide rows are connected to the upper part of the active antenna, the highest heat fluxes are obtained with the LH grill retracted far away from the main plasma. This counter-intuitive behavior is correlated with non-monotonic radial variations of C_{ref} on upper modules in figure 6. Low ΔT_{IR} are obtained near $\delta r = 0$, on waveguide rows connected magnetically to the upper and lower parts of the antenna box.

5. 2D SOL characterization with reciprocating Langmuir probe

So far RF-induced SOL modifications have been probed indirectly, through such indicators as Y_{eff}, C_{ref} or ΔT_{IR}. More direct SOL characterization during ICRF has been performed by

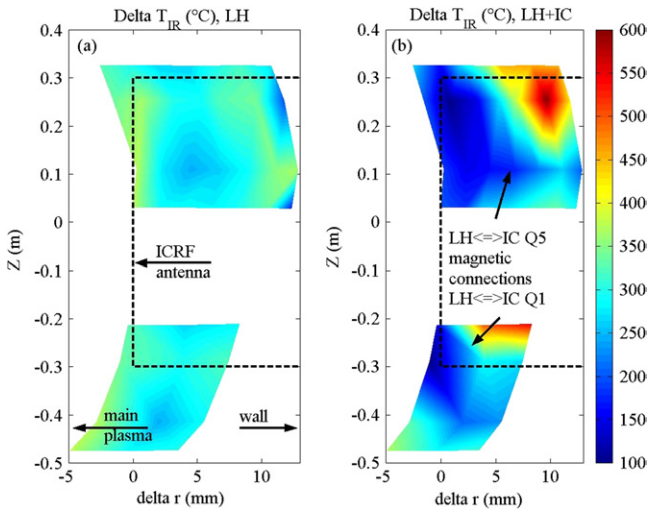

Figure 7. 2D mapping of steady-state temperature elevation on left side limiter of LH grill on TS, in the same coordinate system as on figure 6. (*a*) with LH grill powered alone (1 MW); (*b*) LH grill (1 MW) combined with 1 MW from connected ICRF antenna (either Q1 left or Q5 right to LH grill). Dashed lines: same as figure 6. Same color scale on the two panels.

various techniques in the past [1, 2, 20, 27, 33]. The observed SOL changes were generally interpreted in terms of profile modifications, whereas poloidal inhomogeneity also arises. SOL modifications were therefore mapped in 2D on TS by means of a reciprocating Langmuir probe, combined with $q(a)$ scans through plasma current steps, in order to move vertically the magnetic connection to the ICRF antenna [8]. Over the scan the Faraday screen misalignment on tilted field lines varied between 0° and 3.5°. When the ICRF antenna connected to the probe was powered, localized high positive peaks appeared on the floating potential $V_{\rm float}$. Similar biasing was evidenced in front of the LH launchers [37]. Typical values of the potential (140 V maximum) are of the same order as those inferred from $Y^{\rm eff}$ on AUG. Figure 8 shows that the *ICRF-perturbed zone* is radially centered near $\delta r = 0$, with a radial width of typically 1 cm. $V_{\rm float}$ exhibits strong poloidal variation that is nearly symmetric with respect to the equatorial plane: a local minimum is observed near $Z = 0$ and local maxima near lower and upper parts of the antenna box. In [32] high floating potentials were already measured on field lines passing in front of the TS antenna box corners. At a given (δr, Z) position, some parametric dependences of $V_{\rm float}$ were presented in [8, 18]: a small increase of $V_{\rm float}$ was found with local ICRF power (less than $P_{\rm ICRF}^{1/2}$ expected by the simplest RF-sheath models) and a large decrease with plasma density.

Figure 9 shows that in the *perturbed zone*, the radial variation of the ion saturation current $J_{\rm sat}$ measured by the probe also strongly depends on Z. Near the equatorial plane $J_{\rm sat}$ keeps its value without RF power or even increases. Local minima of $J_{\rm sat}$ were measured near the top and bottom of the antenna box. They were centered near $\delta r = 0$, with a typical radial extension of 1 cm on each side. This coincides with the low temperature zones of figure 6(*b*). The radial variations of $J_{\rm sat}$ are also consistent with non-monotonic behavior of $\Delta T_{\rm IR}$ and $C_{\rm ref}$.

6. Synthesis and outlook

Both sputtering measurements and probe measurements suggest that the local environment of an ICRF antenna gets biased positively. Several theoretical models predict RF-enhanced dc

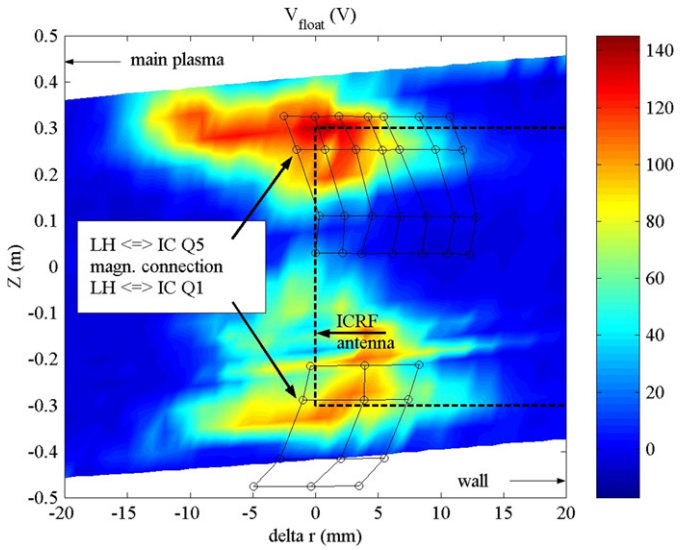

Figure 8. 2D mapping of floating potential measured by reciprocating Langmuir probe on TS, in the same coordinate system as in figure 6. Superimposed: magnetic connections from LH grill to the two neighboring ICRF antennas in figures 6 and 7.

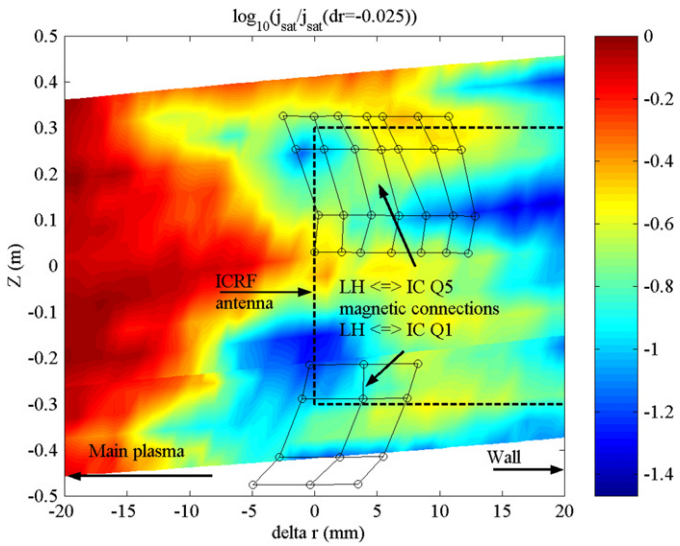

Figure 9. 2D mapping of ion saturation current measured by reciprocating Langmuir probe on TS, in the same coordinate system as in figure 6. The current is normalized to its value in $\delta r = -25$ mm and plotted on a logarithmic scale. Measurements were made with the probe connected to powered antenna Q5 (1.5 MW) [8]. Superimposed: magnetic connections from LH grill to the two neighboring ICRF antennas in figures 6 and 7.

sheath potentials [5, 11, 15, 22, 28, 29]. Within the simplest model [28], or the more elaborate one [15], the relevant quantity for driving the RF-sheaths is $E_{\|\mathrm{RF}}$ integrated along open magnetic field lines. In $[0,\pi]$ strap phasing, this integral was found maximal on long field lines passing in front of the upper and lower parts of the TS [9] and AUG [4] antenna box.

Note however that some measurements were performed not *in front* but *behind* the antenna side limiters. The radial width of the perturbed zone in figures 8 and 9 is of the order of the skin depth c/ω_{pe} for $E_{\|RF}$ at $k_\| = 0$ (typically 8 mm for $n_e = 4.5 \times 10^{17}\,m^{-3}$). $E_{\|RF}$ excitation was attributed to parallel RF currents flowing in the box frame [4, 6] and nearby Faraday screen rods [9]. As originally proposed by [10], $\boldsymbol{E} \times \boldsymbol{B}_0$ drift in the gradient of an inhomogeneous distribution of dc potential produces convective cells. On TS and JET $\boldsymbol{v}_{\boldsymbol{E}\times\boldsymbol{B}}$ is directed upwards on the plasma side of the cells. A typical value of $v_{E\times B} \sim 3.5\,km\,s^{-1}$ was inferred from figure 8, where the plasma potential was assimilated to the measured V_{float} [8]. Convection produces a complicated density pattern [2]: depletion is expected at the centre of the convective cells, while over-density is brought to the top of the antenna and behind the cells. Convection was already suspected on TS from a flip of asymmetric hot spot patterns upon magnetic field reversal [7, 18]. The only way to reconstruct the pattern is 2D (perhaps three dimensions (3D)) mapping. On TS with [0,π] strap phasing, this picture seems consistent with observations both on the LH grill (figures 6 and 7) and on the reciprocating probe (figures 8 and 9). It is worth repeating the same exercise with other antenna geometries or strap phasings, in order to fully correlate the topology of sheath potentials with RF currents paths over different antenna front faces.

Some lessons can already be drawn for ITER. If the models by [28] or [15] turn out to be valid, designs should reduce parallel RF currents on the antenna front face as well as on all nearby metallic components (port, wall, etc) in order to decrease sputtering during ICRF application and improve compatibility with high-Z materials of the first wall. Some design options for the antenna box and the Faraday screen have been examined numerically in [4,6,9]. Global assessment is however needed since all possible paths need to be considered for $j_\|$ all over the antenna front face and the metallic port. Presently it can only be noted that a tilted Faraday screen, even with small misalignment, does not completely suppress SOL modifications. Furthermore high-Z materials should be used with care in the antenna vicinity. LH–ICRF interaction can become critical, especially in the case of poloidal density asymmetry: some LH waveguide rows could experience coupling difficulties while at the same time others could bear excessive heat loads. Interaction can be easily reduced if magnetic connections are minimized by careful port allocation. Presently LH and ICRF launchers are separated by 40° toroidally on ITER, so that magnetic connection is hardly avoidable. An alternative option with 80° toroidal separation could be envisaged. Further, gas injection helps by increasing the local density on LH grills. The exact amount of gas should be determined from a trade-off between reliable LH coupling and reasonable heat fluxes from accelerated electrons and should be applied at the location where the density is depleted.

References

[1] Artemenkov L I *et al* 1988 *Proc. 15th EPS Conf. on Controlled Fusion and Plasma Heating (Dubrovnik, May 1988)* vol 12B(II) p 702

[2] Bécoulet M *et al* 2002 *Phys. Plasmas* **9** 2619–32

[3] Bobkov V V *et al* 2007 *J. Nucl. Mater.* **363–365** 122–6

[4] Bobkov V V *et al* 2007 *Proc. 17th Topical Conf. on RF Power in Plasmas (Clearwater, FL, 2007) AIP Conf. Proc.* **933** 83–6

[5] Carter M D *et al* 1992 *Phys. Fluids* B **4** 1081

[6] Colas L, Heuraux S, Brémond S and Bosia G 2005 *Nucl. Fusion* **45** 767–82

[7] Colas L *et al* 2006 Key results of long pulse ICRH operation in Tore Supra *Nucl. Fusion* **46** S500–13

[8] Colas L *et al* 2007 *J. Nucl. Mater.* **363–365** 555–9

[9] Colas L and Heuraux S 2007 RF-sheath assessment of ICRF Faraday Screens *Proc. 17th Topical Conf. on RF Power in Plasmas (Clearwater, FL, 2007) AIP Conf. Proc.* **933** 215–18

[10] D'Ippolito D A *et al* 1993 *Phys. Fluids* B **5** 3603

[11] D'Ippolito D A and Myra J R 2006 *Phys. Plasmas* **13** 102508
[12] Dux R *et al* 2007 *J. Nucl. Mater.* **363–365** 112–16
[13] Ekedahl A *et al* 2003 *Proc. 15th Topical Conf. on RF Power in Plasmas (Moran, WI, 2003) AIP Conf. Proc.* **694** 259–62
[14] Ekedahl A *et al* 2007 *Proc. 17th Topical Conf. on RF Power in Plasmas (Clearwater, FL, 2007) AIP Conf. Proc.* **933** 237–44
[15] Faudot E *et al* 2006 *Phys. Plasmas* **13** 042512
[16] Fuchs V, Goniche M, Demers Y, Jacquet P and Mailloux J 1996 *Phys. Plasmas* **3** 4023–35
[17] Goniche M *et al* 1998 *Nucl. Fusion* **38** 919
[18] Goniche M *et al* 2006 *Proc. IAEA Conf. (Chengdu, 2006)*
[19] Guilhem D *et al* 2005 *Fusion Eng. Des.* **74** 879
[20] Hanson G R *et al* 1995 *Proc. 11th Topical RF Conf. (Palm Springs)* p 463
[21] Kirov K *et al* 2007 *Proc. 17th Topical Conf. on RF Power in Plasmas (Clearwater, FL, 2007) AIP Conf. Proc.* **933** 257–60
[22] Lieberman M A and Godyak V A 1998 *IEEE Trans. Plasma Sci.* **26** 955
[23] Meyer O *et al* 2007 *Proc. 34th EPS Conf. on Plasma Physics (Warsaw)*
[24] Moreau Ph *et al* 2006 RF heating optimization on Tore Supra using feedback control of infrared measurements *Proc. SOFT 2006 (Warsaw) 2007 Fusion Eng. Des.* at press
[25] Noterdaeme J-M 1991 *Proc. 9th Topical Conf. on RF Power in Plasmas (Charleston, SC, 1991) AIP Conf. Proc.* **244** 71–85
[26] Noterdaeme J-M and Van Oost G 1993 *Plasma Phys. Control. Fusion* **35** 1481 (and references therein)
[27] Noterdaeme J-M *et al* 1996 *23th EPS Conf. Plasma Physics (Kiev, 1996)* vol 20C (ECA) part 2 p723–6
[28] Perkins F W 1989 *Nucl. Fusion* **29** 583
[29] Petržilka V *et al* 2005 *32nd EPS Conf. on Plasma Physics and Controlled Fusion (Tarragona, Spain)* vol 29C (ECA) P-2.095
[30] Petržilka V *et al* 2006 *Proc. 33rd EPS Conf. on Plasma Physics (Rome, 19–23 June 2006)* vol 30I (ECA) P-5.108
[31] Saito K *et al* 2007 *J. Nucl. Mater.* **363–365** 1323–8
[32] Thomas C E *et al* 1996 *Fusion Technol.* **30** 1
[33] Van Oost G *et al* 1990 *Fusion Eng. Des.* **12** 149
[34] Wallace G *et al* 2007 *Proc. 17th Topical Conf. on RF Power in Plasmas (Clearwater, FL, 2007) AIP Conf. Proc.* **933** 277–80
[35] Wukitch S *et al* 2007 *J. Nucl. Mater.* **363–365** 491–7
[36] Wukitch S *et al* 2007 *Proc. 17th Topical Conf. on RF Power in Plasmas (Clearwater, FL, 2007) AIP Conf. Proc.* **933** 75–82
[37] Žaèek F, Petržilka V and Goniche M 2005 *Plasma Phys. Control. Fusion* **47** L17